RESEARCH ARTICLE
SOLID EARTH: GEODYNAMICS

Earth and Planetary Physics
9: 1001–1009, 2025
doi: 10.26464/epp2025055

Primordial hydrogen partitioning at Earth's core–mantle boundary: Multicomponent effects revealed by machine learning-augmented first-principles simulations

ZePing Jiang[1,2], YuYang He[1,2], and ZhiGang Zhang[1,2*]

[1]Key Laboratory of Planetary Science and Frontier Technology, Institute of Geology and Geophysics, Chinese Academy of Sciences, Beijing 100029, China;
[2]College of Earth and Planetary Sciences, University of Chinese Academy of Sciences, Beijing 100029, China

Key Points:

- Oxygen and silicon reduce the siderophile character of hydrogen under core–mantle conditions.
- Countering multicomponent effects revealed lower core hydrogen inventories, reconciling primordial differentiation with present-day geophysical observations.
- Machine learning-augmented first-principles simulations enable precise quantifications of volatiles in more complex systems.

Citation: Jiang, Z. P., He, Y. Y., and Zhang, Z. G. (2025). Primordial hydrogen partitioning at Earth's core–mantle boundary: Multicomponent effects revealed by machine learning-augmented first-principles simulations. *Earth Planet. Phys.*, *9*(5), 1001–1009. http://doi.org/10.26464/epp2025055

Abstract: Hydrogen partitioning between liquid iron alloys and silicate melts governs its distribution and cycling in Earth's deep interior. Existing models based on simplified Fe-H systems predict strong hydrogen sequestration into the core. However, these models do not account for the modulating effects of major light elements such as oxygen and silicon in the core during Earth's primordial differentiation. In this study, we use first-principles molecular dynamics simulations, augmented by machine learning techniques, to quantify hydrogen chemical potentials in quaternary Fe-O-Si-H systems under early core–mantle boundary conditions (135 GPa, 5000 K). Our results demonstrate that the presence of 5.2 wt% oxygen and 4.8 wt% silicon reduces the siderophile affinity of hydrogen by 35%, decreasing its alloy–silicate partition coefficient from 18.2 (in the case of Fe-H) to 11.8 (in the case of Fe-O-Si-H). These findings suggest that previous estimates of the core hydrogen content derived from binary system models require downward revision. Our study underscores the critical role of multicomponent interactions in core formation models and provides first-principles-derived constraints to reconcile Earth's present-day hydrogen reservoirs with its accretionary history.

Keywords: partition coefficient; hydrogen; core–mantle differentiation; light elements; machine learning; density functional theory

1. Introduction

Hydrogen, as the most active volatile element in Earth's system, plays important roles in a spectrum of geochemical processes, including hydrogen incorporation in mantle minerals (e.g., Pearson et al., 2014; Zhou SY, 2025), water–rock interactions in subduction zones (e.g., Hacker, 2008; Pan CC, 2023), hydrogen-induced mantle melting (e.g., Hirschmann, 2006), and light-element alloying in the core (e.g., Okuchi, 1997). Although the surficial cycling of hydrogen has been studied extensively, its deep Earth inventory remains one of the most elusive components of global volatile budgets. Recent studies have proposed that the core might constitute Earth's primary hydrogen reservoir, potentially storing >90% of the planet's primordial hydrogen through early accretion processes (Li YG et al., 2020; Hirose et al., 2021; Broadley et al. 2022). This immense sequestration likely occurred during core–mantle differentiation, when molten iron segregated through a magma ocean. Incorporating hydrogen as a key light element continues to shape core dynamics through its effects on density, thermal conductivity, and outer core convection (Umemoto and Hirose, 2015, 2020; Hirose et al.,2013, 2021).

The primary constraints on hydrogen distribution between geochemical reservoirs fundamentally depend on its partitioning coefficients at major interfaces. Quantifying the primordial incorporation of hydrogen into the core requires a precise determination of its alloy–silicate partition coefficient ($D_H^{alloy/silicate}$) at the core–mantle boundary (CMB) (Zhang YG et al., 2012). However, the small neutron scattering cross-section of hydrogen makes experimental detection challenging, especially under high-pressure conditions (Kuramoto and Matsui, 1996). Most existing experiments have been conducted at pressures below 20 GPa, resulting in divergent perspectives on whether hydrogen exhibits siderophile (Okuchi, 1997; Shibazaki et al., 2009) or lithophile (Clesi et al., 2018; Malavergne et al., 2019) characteristics. Notably,

First author: Z. P. Jiang, jiangzeping22@mails.ucas.ac.cn
Correspondence to: Z. G. Zhang, zgzhang@mail.iggcas.ac.cn
Received 03 MAR 2025; Accepted 08 APR 2025.
First Published online 23 JUN 2025.

Malavergne et al. (2019) observed a pressure-dependent transition in hydrogen partitioning behavior, changing from lithophile to siderophile at >15 GPa. Additionally, Clesi et al. (2018) attributed their observed hydrogen's lithophilic tendency in response to the presence of coexisting carbon in the experimental system. These findings underscore the necessity of further investigating hydrogen partition coefficients across broader pressure–temperature (P–T) ranges and in multicomponent systems with coexisting light elements.

Previous first-principles studies have revealed strong siderophile characteristics of hydrogen in Fe-H systems at 135 GPa (Li YG et al., 2020). However, these binary Fe-H models omitted critical interactions with oxygen and silicon, which are the predominant light elements in CMB chemistry (Badro et al., 2014, 2015; Hirose et al., 2017). Under magma ocean conditions, the oxygen/silicon concentrations in iron melts can reach 5–10 wt% (Fischer et al., 2015), significantly influencing the chemical behavior of hydrogen. This omission is largely attributed to the substantial computational cost of multicomponent first-principles molecular dynamics (FPMD). In such simulations, both system size and the required timescale increase exponentially with compositional complexity. Consequently, existing models do not adequately describe the multicomponent effects of other light elements on the behavior of hydrogen.

To overcome this limitation, we developed a machine learning (ML)-augmented computational framework to explore hydrogen partitioning behavior under realistic CMB conditions, considering the most abundant light elements, oxygen and silicon, with nonstoichiometric H/O ratios. This approach combined three computational components: (1) first-principles electronic structure calculations; (2) neural network potentials trained on multicomponent datasets to achieve near-density functional theory (DFT) accuracy at a computational cost of 1/1000th that of standard FPMD simulations; and (3) thermodynamic integration schemes optimized for extreme P–T conditions (Wang H et al., 2018; Zhang ZG et al., 2020). This integrated workflow facilitated efficient exploration of diverse thermodynamic regimes, including varying P–T paths and melt compositions. With their focus on the primordial CMB environment, our quaternary Fe-O-Si-H system simulations indicated that the presence of oxygen and silicon reduced the siderophile tendency of hydrogen. This result demonstrates that the multicomponent effects should be adequately counted in the modeling of Earth's core accretion.

2. Methods

2.1 First-Principles Electronic Structure Calculations

First-principles electronic structure calculations were used to generate high-accuracy and representative training datasets for both the liquid iron alloy and the molten silicate systems. These datasets were subsequently used to train neural network potential models for each system. The trained potential models were then applied to perform molecular dynamics (MD) simulations tailored for thermodynamic integration, which enabled the calculation of free energy data. We first conducted low-accuracy FPMD simulations for the systems under investigation. From these simulations, we randomly extracted a subset of configurations with sufficient diversity, which were then subjected to high-accuracy electronic structure calculations.

In the liquid iron alloy system, we considered fixed oxygen and silicon proportions ($Fe_{74}O_{15}Si_8H_n$). The composition of $Fe_{74}O_{15}Si_8$ was directly chosen based on previous studies that constrained the concentrations of light elements in the Earth's core (Hirose et al., 2021), and both oxygen and silicon were approximately 5 wt%. At 135 GPa and 5000 K, this amount of oxygen and silicon in the iron alloy did not exceed the exsolution limit of SiO_2 (Zhang ZG et al., 2022a), and the system remained in a miscible liquid phase. The hydrogen content varied from 0 to 15 atomic percent (at%), which spans the hydrogen content in the Earth's core constrained by geophysical observations (Hirose et al., 2021). In the molten silicate phase, we adopted a bridgmanite-based composition ($Mg_{40}Si_{40}O_{120}H_n$) as an approximation of the lower mantle (Garnero et al., 2016) and varied the hydrogen content from 0 to 10 at%. The temperature and pressure were fixed at 5000 K and 135 GPa. The incorporation of magnesium in iron alloys or iron in silicate melts was not explicitly considered because its effect was negligible for the purposes of this investigation (Zhang ZG et al., 2022b).

Electronic structure calculations were performed using the DFT-based software Vienna Ab initio Simulation Package (VASP), employing the projector augmented-wave method (Kresse and Joubert, 1999) and pseudopotentials in the Perdew–Burke–Ernzerh functional form of the generalized gradient approximation (Perdew et al., 1996). First, each system underwent relatively low-accuracy FPMD simulations to sufficiently explore the configurational space. For this purpose, pseudopotentials with a smaller cutoff were chosen to minimize sampling costs. The plane–wave cutoff (ENCUT) was set at 500 eV, and the convergence criterion for electronic structure iterations (EDIFF) was set at 1×10^{-4} eV. The simulations were performed in the canonical (NVT) ensemble with a Nosé thermostat. In total, 12 simulations were performed for the liquid iron systems and 26 simulations were performed for the silicate systems, yielding more than 300,000 and 500,000 meaningful configurations, respectively.

A subset of configurations were then randomly selected from the sampled structures for high-accuracy calculations. To achieve greater precision, we used a pseudopotential for iron with 16 valence electrons (valence configuration $3s^23p^63d^74s^1$), which is essential for accurately modeling iron properties in the Earth's core (Sun T et al., 2018). Additionally, we used pseudopotentials with higher cutoff energies for both oxygen and hydrogen. The ENCUT was set at 900 eV, and the EDIFF was set at 1×10^{-6} eV. The Mermin functional was used to account for finite temperature effects (Mermin, 1965), with electron occupancy treated by using Fermi–Dirac smearing, and the electronic temperature was set as equal to the ionic temperature. The resulting high-accuracy energy and force data were subsequently used to train the neural network potential model.

2.2 Neural Network Potentials

Calculating Helmholtz free energy requires extensive sampling of the system's phase space, which makes direct FPMD simulations prohibitively expensive. Machine learning-based approaches for generating interatomic potentials have been shown to effectively

address the longstanding trade-off between accuracy and efficiency in MD simulations (Mueller et al., 2020; Zhang ZG et al., 2020). In this study, we used the open-source software package DeePMD-kit (Wang H et al., 2018; Zeng JZ et al., 2023) to develop accurate and transferable artificial neural network machine learning (ANN-ML) potential models under CMB conditions for molten silicates and liquid iron alloys, respectively. These models enable reliable MD simulations of materials under the high-pressure and high-temperature conditions of the Earth's CMB.

A Deep Potential model uses an atom-centered framework to model interatomic potentials. The input layer processes atomic structural data, and the output layer generates the atomic energy E_i for each atom. The total potential energy E of an atomic structure is calculated by summing the atomic energies. In this study, we utilized the Deep Potential Smooth Edition (DeepPot-SE) model (Zhang LF et al., 2018) implemented in the DeePMD-kit software package to develop the ANN-ML interatomic potential. The DeepPot-SE model incorporates all angular and radial information from atomic configurations. Its input descriptors comprise two main components: an environment matrix and an embedding matrix. The environment matrix encodes local geometry, including neighbor positions, distances, and a switching function designed to smoothly exclude atoms beyond the cutoff radius. The embedding matrix applies a neural network for nonlinear mapping of the environment data, thereby capturing intricate many-body interactions. These descriptors are then optimized and trained through the neural network, enabling the development of a robust and accurate interatomic potential (Zeng JZ et al., 2023).

In both the liquid iron alloy and molten silicate potential models, the cutoff radius (r_c) was set to 6.5 Å, with descriptors smoothly decaying between 6.0 Å (r_{cs}) and 6.5 Å. The filter and fitting neural networks were configured with sizes (25, 50, 100) and (240, 240, 240) respectively, whereas the axis neuron was set to 16. The learning rate decreased exponentially from an initial value of 0.001, with a decay step of 5000, and total training steps of 3,000,000 were performed. The loss function included terms for energy, ionic forces, and system stress. Initially, the training emphasized force learning, then gradually shifted to focus on energy and stress. The weighting coefficients were defined as $p_\varepsilon^{\rm start} = 0.02$, $p_\varepsilon^{\rm limit} = 1$, $p_f^{\rm start} = 1000$, $p_f^{\rm limit} = 1$, $p_v^{\rm start} = 0.02$, $p_v^{\rm limit} = 1$. To train the potential models, 1200 high-accuracy electronic structure configurations were used for the liquid iron alloy, and 1600 were used for the molten silicate. During validation, the alloy and silicate models were tested on datasets containing 200 and 300 configurations, respectively. The alloy model yielded a root mean square error (RMSE) of ~6.6 meV/atom for energy, ~0.34 eV/Å for force, and ~2.9 eV/Å^3 for stress (Figure S1). The silicate model yielded an RMSE of ~12.7 meV/atom for energy, ~0.43 eV/Å for force, and ~7.3 eV/Å^3 for stress (Figure S2).

2.3 Thermodynamic Integration

We rigorously calculated the Helmholtz free energy by using the thermodynamic integration method (Zhang ZG et al., 2020). This technique determines the free energy difference between a real system B and the reference system A by introducing a continuum of intermediate states:

$$\Delta F_{\rm AB} = \int_0^1 \left\langle \frac{\partial U}{\partial \lambda} \right\rangle_\lambda {\rm d}\lambda, \tag{1}$$

where $U(r_1, r_2, \ldots, r_N, \lambda) \equiv f(\lambda) U_{\rm A}(r_1, r_2, \ldots, r_N) + g(\lambda) U_{\rm B}(r_1, r_2, \ldots, r_N)$, where $f(\lambda)$ and $g(\lambda)$ are switching functions. For the purposes of this study, we selected $f(\lambda) = \lambda$ and $g(\lambda) = 1 - \lambda$. The notation $\langle \ldots \rangle_\lambda$ represents the ensemble average over the intermediate state λ.

In practice, the thermodynamic integration formula was implemented as follows: a set of λ values were selected from the interval [0, 1]. For each chosen $\lambda_{\rm k}$ value, a full MD simulation was performed to compute the corresponding average $\langle \partial U/\partial \lambda_{\rm k} \rangle_{\lambda_{\rm k}}$. The free energy difference $\Delta F_{\rm AB}$ was obtained through numerical integration (Tuckerman, 2023). In this study, the $\{\lambda_{\rm k}\}$ values were chosen based on Gauss–Lobatto quadrature nodes, a selection that improves the convergence of the integration (Zwillinger, 2002; Zhang ZG et al., 2020). We included 7 abscissas ($n = 7$) in practice.

For both the liquid iron alloy phase and the molten silicate phase, we selected an ideal gas with the same composition and temperature as the reference system. The Helmholtz free energy of the ideal gas can be rigorously calculated by using the following formula:

$$F_0^{\rm alloy} = -k_{\rm B}T \ln\left(\frac{V^{N_{\rm Fe}+N_{\rm O}+N_{\rm Si}+N_{\rm H}}}{N_{\rm Fe}!N_{\rm O}!N_{\rm Si}!N_{\rm H}!\Lambda_{\rm Fe}^{3N_{\rm Fe}}\Lambda_{\rm O}^{3N_{\rm O}}\Lambda_{\rm Si}^{3N_{\rm Si}}\Lambda_{\rm H}^{3N_{\rm H}}} \right), \tag{2}$$

$$F_0^{\rm silicate} = -k_{\rm B}T \ln\left(\frac{V^{N_{\rm Mg}+N_{\rm Si}+N_{\rm O}+N_{\rm H}}}{N_{\rm Mg}!N_{\rm Si}!N_{\rm O}!N_{\rm H}!\Lambda_{\rm Mg}^{3N_{\rm Mg}}\Lambda_{\rm Si}^{3N_{\rm Si}}\Lambda_{\rm O}^{3N_{\rm O}}\Lambda_{\rm H}^{3N_{\rm H}}} \right), \tag{3}$$

where $\Lambda = h/\sqrt{2\pi M k_{\rm B} T}$ is the thermal wavelength of the specific element (h is Planck's constant, N is the number of atoms, $k_{\rm B}$ is Boltzmann's constant, M is the atomic mass, and T is the temperature). In practice, Stirling's approximation $\ln N! \approx N\ln N - N$ was used. With the Helmholtz free energy difference ΔF and the reference F_0 obtained, F was calculated as $F = F_0 + \Delta F$. The Gibbs energy of the system could then be calculated as $G = F + P_0 V$, where P_0 is the target pressure and V is the volume of the simulated system.

When calculating the free energy by thermodynamic integration, we performed MD sampling under the canonical ensemble with a Large-scale Atomic/Molecular Massively Parallel Simulator (Thompson et al., 2022). During the simulations, we used neural network potentials that were previously trained separately for the liquid alloy and silicate systems. We selected six composition points in the Fe-O-Si-H alloy phase and nine composition points in the silicate phase, all within a hydrogen atomic fraction range of 0–20 at% (Table S1). For comparison, we also calculated five composition points for the Fe-H alloy (Figure S3). To reduce statistical errors arising from thermal fluctuations, we increased the simulation cell size compared with the first-principles stage. Specifically, the Fe-O-Si-H systems were expanded to contain 8 times the number of atoms in a single $Fe_{74}O_{15}Si_8H_n$ unit cell, whereas the silicate melt systems were enlarged to 4 times the number of atoms in a $Mg_{40}Si_{40}O_{120}H_n$ unit cell. The corresponding molar volume parameters are presented in Table S1. At high temperatures and pressures, atomic motion becomes highly vigorous, especially in systems containing light elements such as hydrogen. To accurately capture the behavior of these light elements, a time step of 0.1 fs was utilized. At each composition point, a full MD sampling was performed at each of the seven

Gaussian quadrature nodes, with each MD simulation consisting of 300,000 steps, corresponding to a simulation time of 30 ps. In total, 154 simulations were deployed to obtain the thermodynamic data reported in Table S1.

2.4 Thermodynamics for Calculating the Partition Coefficient

By definition, the chemical potential of hydrogen is its partial molar Gibbs energy:

$$\mu_{\mathrm{H}}^{\mathrm{alloy/silicate}}(P,T,x)=\left(\frac{\partial G}{\partial n_{\mathrm{H}}^{\mathrm{alloy/silicate}}}\right)_{P,T,n_{\mathrm{Fe,O,Si}}/n_{\mathrm{Mg,Si,O}}}. \tag{4}$$

In this study, the pressure and temperature were fixed at 135 GPa and 5000 K, respectively. As a result, the chemical potential of hydrogen became solely a function of the composition x, which is defined as the stoichiometric number of hydrogen atoms in the formula $(Fe_{74}O_{15}Si_8)_{1-x}H_x$ for alloy systems and $(Mg_{40}Si_{40}O_{120})_{1-y}H_y$ for silicate systems.

The Gibbs energy can be obtained from thermodynamic integration, but directly calculating the chemical potential of hydrogen based on its definition may involve substantial errors. To address this issue, we implemented the following regularization method (Pozzo et al., 2019; Li YG et al., 2019, 2020). First, we expressed the Gibbs energy and chemical potential as follows:

$$G(P,T,x)=\overline{G}(P,T,x)-TS_{\mathrm{mix}}^{\mathrm{system}}, \tag{5}$$

where $TS_{\mathrm{mix}}^{\mathrm{system}}$ represents the contribution of the ideal mixing entropy, which can be calculated analytically, and $\overline{G}(P,T,x)$ represents the pure component Gibbs energy. The $\overline{G}(P,T,x)$ is related to the pure component chemical potential by $\overline{G}=\sum_{i=1}^{n}x_i\overline{\mu}_i$, where x_i is the mole fraction of the ith component. We obtained G per the formula for different x values through thermodynamic integration and calculated the corresponding $\overline{G}$. It was observed that $\overline{G}$ could be linearly fitted by $\overline{G}=a+bx$. The pure component chemical potential $\overline{\mu}$ could then be directly obtained as follows:

$$\overline{\mu}(P,T,x)=\overline{G}(P,T,x)+(1-x)\left(\frac{\partial\overline{G}(p,T,x)}{\partial x}\right)=a+b. \tag{6}$$

The chemical potential is denoted as $\mu(P,T,x)=\overline{\mu}(P,T,x)-TS_{\mathrm{mix}}^{\mathrm{H}}$, where $S_{\mathrm{mix}}^{\mathrm{H}}$ represents the contribution of the mixing behavior of the hydrogen component to the total system entropy. This can be expressed as $S_{\mathrm{mix}}^{\mathrm{system}}+(1-x)\left(\frac{\partial S_{\mathrm{mix}}^{\mathrm{system}}}{\partial x}\right)$.

In this study, the ideal mixing entropy of alloy systems and silicate systems, respectively, are as follows:

$$S_{\mathrm{mix}}^{(Fe_{74}O_{15}Si_8)_{1-x}H_x}=-k_{\mathrm{B}}\cdot(97-96x)\cdot(x_{\mathrm{Fe}}\ln x_{\mathrm{Fe}}+x_{\mathrm{O}}\ln x_{\mathrm{O}}+x_{\mathrm{Si}}\ln x_{\mathrm{Si}}+x_{\mathrm{H}}\ln x_{\mathrm{H}}),$$

where $x_{\mathrm{Fe}}=\frac{74\cdot(1-x)}{97-96x}$, $x_{\mathrm{O}}=\frac{15\cdot(1-x)}{97-96x}$, $x_{\mathrm{Si}}=\frac{8\cdot(1-x)}{97-96x}$, $x_{\mathrm{H}}=\frac{x}{97-96x}$, and

$$S_{\mathrm{mix}}^{(Mg_{40}Si_{40}O_{120})_{1-y}H_y}=-k_{\mathrm{B}}\cdot(200-199y)\cdot(y_{\mathrm{Mg}}\ln y_{\mathrm{Mg}}+y_{\mathrm{Si}}\ln y_{\mathrm{Si}}+y_{\mathrm{O}}\ln y_{\mathrm{O}}+y_{\mathrm{H}}\ln y_{\mathrm{H}}),$$

where $y_{\mathrm{Mg}}=y_{\mathrm{Si}}=\frac{40\cdot(1-y)}{200-199y}$, $y_{\mathrm{O}}=\frac{120\cdot(1-y)}{200-199y}$, $y_{\mathrm{H}}=\frac{y}{200-199y}$.

Then the chemical potential of hydrogen in the liquid iron alloy and the silicate phases is as follows:

$$\mu_{\mathrm{H}}^{\mathrm{alloy}}(P,T,x_{\mathrm{H}})=\overline{\mu}_{\mathrm{H}}^{\mathrm{alloy}}(P,T,x_{\mathrm{H}})-T\left[S_{\mathrm{mix}}^{(Fe_{74}O_{15}Si_8)_{1-x}H_x}+(1-x_{\mathrm{H}})\left(\frac{\partial S_{\mathrm{mix}}^{(Fe_{74}O_{15}Si_8)_{1-x}H_x}}{\partial x}\right)\right] \tag{7}$$

and

$$\mu_{\mathrm{H}}^{\mathrm{silicate}}(P,T,y_{\mathrm{H}})=\overline{\mu}_{\mathrm{H}}^{\mathrm{silicate}}(P,T,y_{\mathrm{H}})-T\left[S_{\mathrm{mix}}^{(Mg_{40}Si_{40}O_{120})_{1-y}H_y}+(1-y_{\mathrm{H}})\left(\frac{\partial S_{\mathrm{mix}}^{(Mg_{40}Si_{40}O_{120})_{1-y}H_y}}{\partial y}\right)\right], \tag{8}$$

respectively.

The migration of hydrogen atoms between the liquid iron alloy and the silicate phase reaches dynamic equilibrium when the chemical potential of hydrogen in both phases is equal. Then the partition coefficient $D^{\mathrm{alloy/silicate}}=c_{\mathrm{H}}^{\mathrm{alloy}}/c_{\mathrm{H}}^{\mathrm{silicate}}$, where c_{H} represents the concentration expressed in atomic percentage. Its relationship with the stoichiometric coefficient is $x_{\mathrm{H}}=1/[1+(1/c_{\mathrm{H}})]$. Therefore, calculating the partition coefficient for hydrogen involves solving the chemical potential equation $\mu_{\mathrm{H}}^{\mathrm{alloy}}\left(P,T,c_{\mathrm{H}}^{\mathrm{alloy}}\right)=\mu_{\mathrm{H}}^{\mathrm{silicate}}\left(P,T,c_{\mathrm{H}}^{\mathrm{silicate}}\right)$ after separately fitting the chemical potential curves of hydrogen in liquid iron and molten silicate. This method for determining partitioning coefficients is grounded in fundamental thermodynamics, and its key advantage lies in efficiently narrowing the composition sampling space. It can be directly extended to more realistic and complex core composition systems.

3. Results and Discussion

3.1 Free Energy Calculations

In the liquid alloy system, as the hydrogen content increases, the Gibbs energy of the system decreases at first (Figure 1a). At this stage, the chemical potential of hydrogen is lower than the average chemical potential of the system, reaching its minimum when it becomes equal to the average chemical potential of the system and then begins to increase. A similar trend is observed in the molten silicate system, where the Gibbs energy decreases first before increasing (Figure 1b). The derived pure component Gibbs energy $\overline{G}$ follows a near-perfect linear trend as a function of the stoichiometric coefficient x (Figures 1c and 1d), indicating that hydrogen atoms are nearly ideally mixed with the Fe-O-Si solvent in the system (see Section 2.4). At 135 GPa and 5000 K, the chemical potential of hydrogen in both the liquid alloy and molten silicate systems exhibits a logarithmic shape (Figure 2a). From a thermodynamic perspective, the chemical potential of hydrogen in the liquid alloy is consistently lower than that in the molten silicate phase, indicating a preferential partitioning of hydrogen into the liquid iron alloy within the Earth's core, thus illustrating its siderophile behavior. Moreover, the chemical potential of hydrogen in the Fe-O-Si-H alloy is generally higher than that in the Fe-H alloy, implying that the presence of oxygen and silicon raises the chemical potential of hydrogen, consequently weakening its siderophile character.

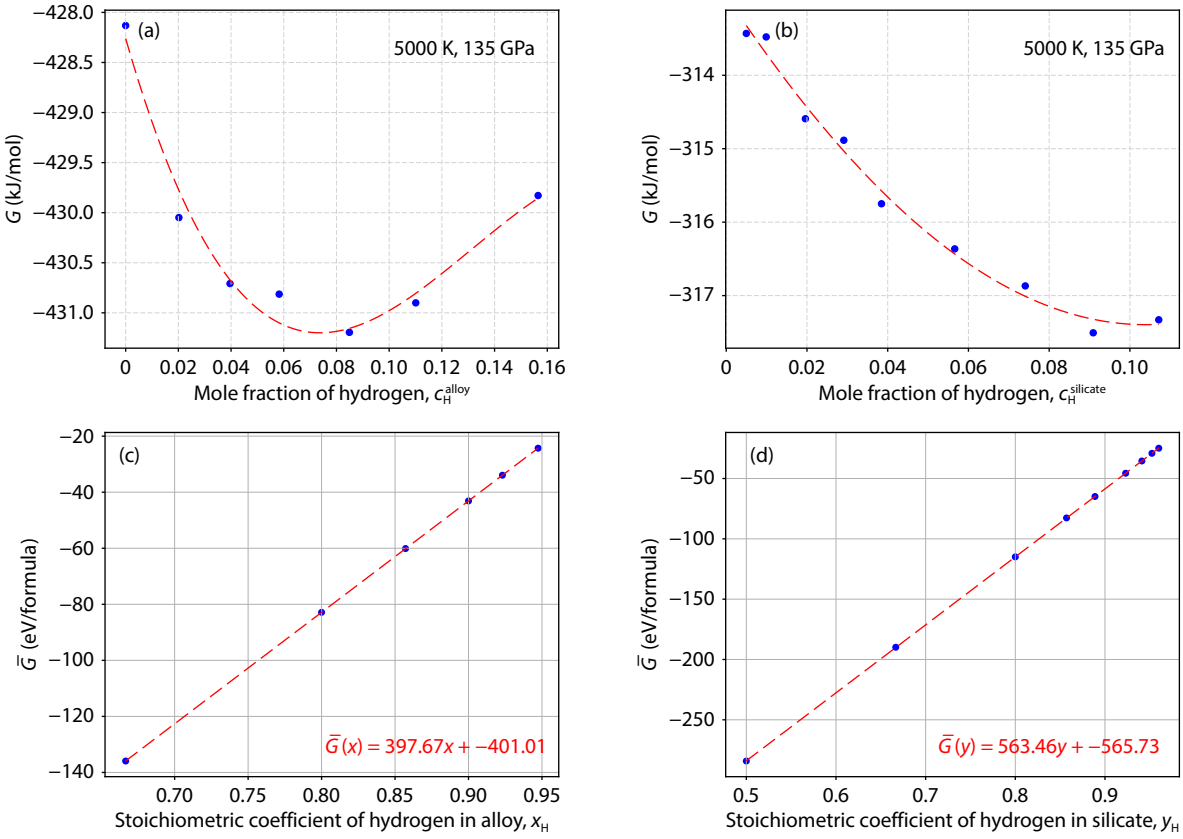

Figure 1. Gibbs energy curves as functions of the hydrogen atomic fraction for (a) the liquid iron alloy systems and (b) the molten silicate systems. The derived pure component Gibbs energy as functions of the stoichiometric coefficient of hydrogen in the formula (c) $(Fe_{74}O_{15}Si_8)_{1-x}H_x$ for alloy systems and (d) $(Mg_{40}Si_{40}O_{120})_{1-y}H_y$ for silicate systems.

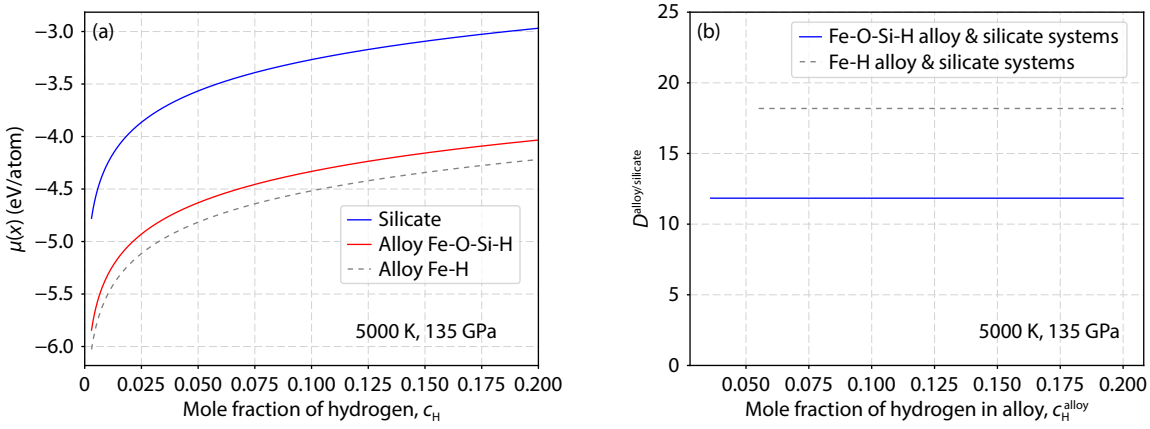

Figure 2. (a) Chemical potential curves as functions of the hydrogen atomic fraction. (b) Partitioning coefficients of hydrogen between the alloy and silicate phase under the condition of the early core–mantle boundary.

3.2 Partitioning Coefficients

Our simulations under conditions of 135 GPa and 5000 K for the Fe-H system without oxygen and silicon yielded $D_H^{alloy/silicate}$ = 18.2, whereas for the Fe-O-Si-H system, this value decreased to 11.8 (Figure 2b). These values remained consistent across hydrogen concentrations of 0–20 at% in the iron alloy. This result suggests that hydrogen still exhibits strong siderophile behavior at higher temperatures but that the introduction of oxygen and silicon substantially reduces its siderophile character.

The spatial distribution of other elements around iron and hydrogen atoms in the Fe-O-Si-H alloy systems, as demonstrated by the radial distribution function (RDF; Figures 3a and 3b), explains the observed trend for $\overline{G}$. From the perspective centered on iron atoms (Figure 3a), the RDFs of hydrogen and oxygen/silicon atoms exhibits a pronounced peak at the nearest neighbor distance (around 2 Å). In contrast, from the hydrogen-centered perspective (Figure 3b), only the RDF of iron atoms shows a peak at the nearest neighbor distance. This result indicates that in the liquid alloy system, both hydrogen and oxygen/silicon atoms

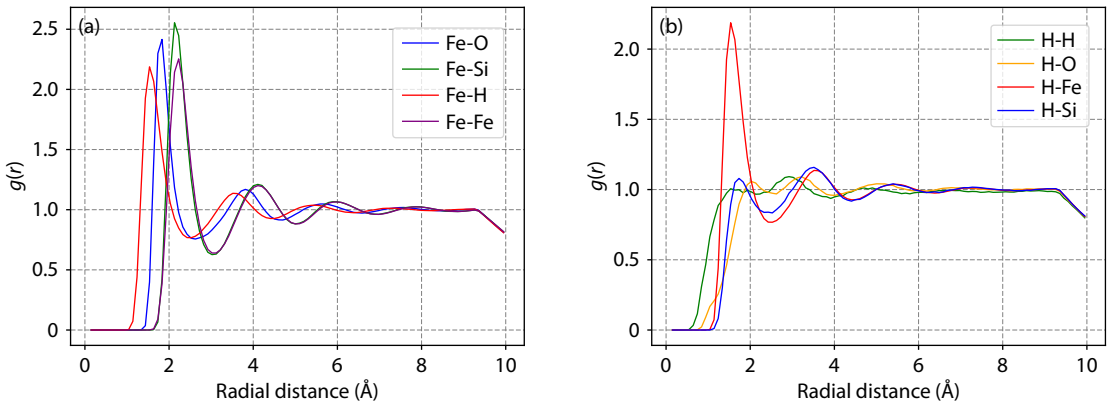

Figure 3. The radial distribution functions in multicomponent iron alloy systems, viewed from the perspectives of (a) iron atoms and (b) hydrogen atoms as the central species.

energetically prefer proximity to iron atoms, whereas hydrogen atoms exhibit no affinity toward oxygen or silicon atoms. This finding suggests that the presence of oxygen and silicon introduces spatial competition with the hydrogen–iron interaction, which consequently elevates the chemical potential of hydrogen in the alloy phase, ultimately weakening its siderophile tendency. Because hydrogen, oxygen, and silicon in the liquid iron alloy all tend to associate with iron to achieve energetically favorable configurations—rather than preferentially interacting with each other—we consider that the Si/O ratio does not significantly affect the simulation results. It should be noted that in the calculation of the hydrogen partition coefficient at 50 GPa and 3500 K using a coexisting simulation, Li YG et al. (2020) observed a significantly lower $D_{\mathrm{H}}^{\mathrm{Fe/MgSiO_3}}$ value of 3.1 ± 0.3 compared with their simplified free energy method of 9.1^{+18}_{-6}. They speculated that this discrepancy could be attributed to the diffusion of trace silicon and oxygen atoms into the iron alloy. Although the thermodynamic conditions differed, our study supports their hypothesis: the presence of dissolved oxygen and silicon in the iron melt noticeably reduces the siderophile character of hydrogen. Additionally, for the Fe-H system, Li YG et al. (2020) reported a partition coefficient $D_{\mathrm{H}}^{\mathrm{Fe/MgSiO_3}}$ of approximately 17 at 135 GPa and 4200 K. Considering the associated uncertainties, this value is comparable to the value of 18.2 obtained in our study at 135 GPa and 5000 K. Although methodological differences could lead to discrepancies, these results indicate that temperature plays a minor role in the siderophile behavior of hydrogen.

3.3 Implications

The storage of light elements such as hydrogen, carbon, oxygen, sulfur, and silicon in the core systematically modifies its seismic velocity profiles, electrical conductivity, and thermodynamic properties. Current models of the core composition remain debated and fail to fully reconcile observed density deficits and seismic anomalies (Badro et al., 2015; Hirose et al., 2017; Tkalčić and Phạm, 2018). The assumption that hydrogen alone could explain these geophysical discrepancies would require a hydrogen content of 1 wt% in the outer core, which is equivalent to approximately 130 ocean masses of water (Umemoto and Hirose, 2015). However, Li YG et al. (2020) showed that even the most optimistic estimates of the siderophile character of hydrogen cannot account for such enrichment. Our research suggests that by considering oxygen and silicon, hydrogen incorporation into the core would be suppressed by an additional 35%, further limiting its abundance. Moreover, if other light elements such as carbon and sulfur within the liquid outer core similarly compete with hydrogen for binding with iron, such competitive dissolution would progressively weaken the siderophile character of hydrogen. Therefore, a comprehensive model that jointly considers multiple light elements is essential to ultimately constrain the composition of the Earth's core.

Furthermore, the estimates of light element concentrations in the core, which are based on metal–silicate partitioning data, intrinsically depend on assumptions regarding mantle abundances and core formation models. Both factors have considerable uncertainties. In the case of hydrogen, its high volatility necessitates considering the contributions of other light elements first. From this perspective, Hirose et al. (2021) proposed that the possible compositional range of the liquid core—Fe + 5% Ni + 1.7% S + 0%–4.0% Si + 0.8%–5.3% O + 0.2% C + 0%–0.26% H by weight—could be consistent with geophysical observations. Notably, this hydrogen estimate approaches the lower bound of previous constraints inferred from metal–silicate partitioning (Li YG et al., 2020; Tagawa et al., 2021), which have suggested that the core incorporated 0.3–0.6 wt% of hydrogen. Our results suggest that when considering the copresence of oxygen and silicon, and if approximately 700 ppm of water remained in a primordial magma ocean (Tagawa et al., 2021), the hydrogen content in the core would be approximately 0.2 wt%, thus providing a potential explanation for this discrepancy. This result underscores the necessity of incorporating multielement interactions in core formation models to achieve a self-consistent explanation of Earth's present-day hydrogen budget.

4. Conclusions

We present a computational framework capable of quantifying the partitioning behavior of volatile elements in multicomponent systems under extreme conditions. This framework addresses critical limitations in modeling Earth's core formation processes. By integrating FPMD, machine-learned interatomic potentials optimized for large compositional spaces, and thermodynamic integration schemes, this methodology enables accurate free energy calculations in quaternary Fe-O-Si-H systems at CMB conditions. The incorporation of an ML approach not only accelerates large-

scale compositional sampling but also captures subtle details of interelement interactions, achieving an accuracy comparable to pure first-principles methods.

Our calculation results suggest that the partitioning of hydrogen between molten alloy and silicate melts is strongly influenced by the presence of oxygen and silicon in the metallic phase. This leads to a 35% decrease in the hydrogen partition coefficient ($D_{\mathrm{H}}^{\mathrm{Fe/MgSiO_3}}$) in the quaternary Fe-O-Si-H system (11.8) compared with the prediction for the binary Fe-H system (18.2). This weakened siderophile character can be attributed to the competition between oxygen, silicon, and hydrogen for bonding with iron atoms, as demonstrated by the RDF analysis. These multicomponent interactions suggest that traditional binary-system models may systematically overestimate the hydrogen sequestration in Earth's core under realistic magma ocean conditions.

Beyond hydrogen, our framework can be expanded to other volatile elements, such as the carbon, nitrogen, and sulfur present in multiphase systems under extreme P–T conditions. This ML-enhanced design enables the efficient exploration of diverse geochemical scenarios, such as varying oxygen fugacity environments during multistage core formation or the interiors of volatile-rich exoplanets analogous to the core of Mars (Stähler et al., 2021; Samuel et al., 2023). In these settings, complex elemental interactions may similarly affect core composition and volatile retention. By bridging the gap between computational scalability and geochemical realism, this work provides a robust foundation for modeling volatile cycling throughout Earth's history and in other celestial bodies.

Acknowledgments

This work was supported by the National Key R&D Program of China (Grant No. 2022YFF0503203), National Natural Science Foundation of China (NSFC) projects (Grant Nos. 42441826 and 42173041), and the Key Research Program of the Institute of Geology and Geophysics, Chinese Academy of Sciences (Grant No. IGGCAS-202204). Simulations were carried out at the computational facilities of the Computer Simulation Laboratory at IGGCAS and the Beijing Super Cloud Computing Center (BSCC).

Supplementary Materials

Appendix A. Supplementary Data

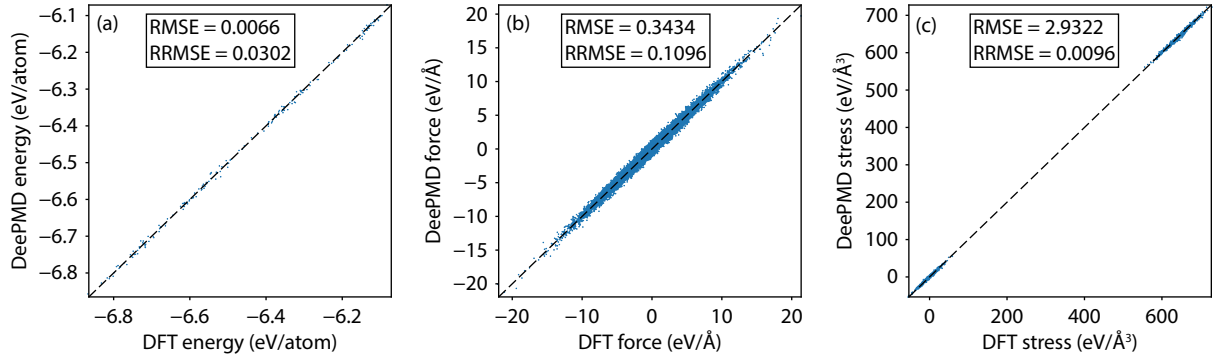

Figure S1. Benchmarks of the Deep Potential model of Fe-O-Si-H alloy liquid systems at 5000 K, 135 GPa. Comparisons of atomic energies (a), forces (b), and stresses (c) between DFT and the Deep Potential model. The test data shown in the figure were completely excluded from the training process and thus form an independent validation set. In total, 180 energies, 59,040 forces, and 1620 normal stress components were included in these comparisons. RMSE, root mean square error; RRMSE, relative root mean square error.

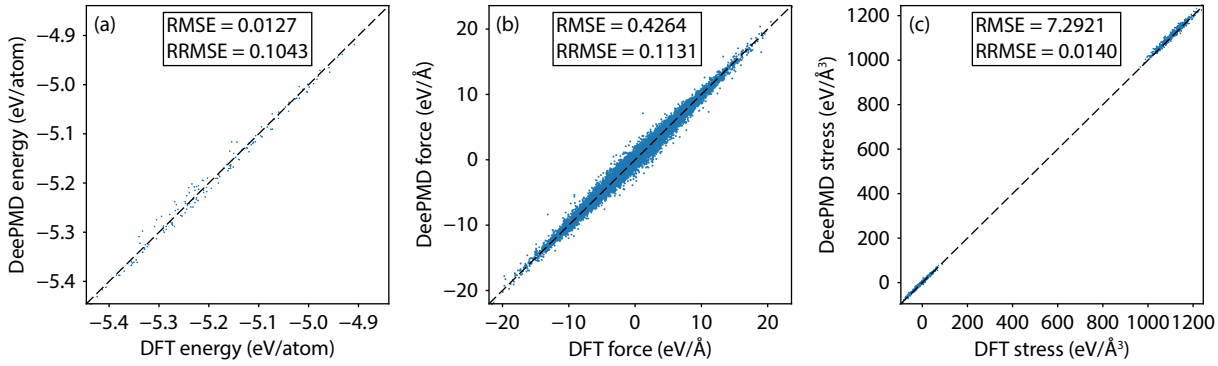

Figure S2. Benchmarks of the Deep Potential model of Mg-Si-O-H silicate melt systems at 5000 K, 135 GPa. Comparisons of atomic energies (a), forces (b), and stresses (c) between DFT and the Deep Potential model. The test data shown in the figure were completely excluded from the training process and thus form an independent validation set. In total, 150 energies, 98,100 forces, and 1350 normal stress components were included in these comparisons. RMSE, root mean square error; RRMSE, relative root mean square error.

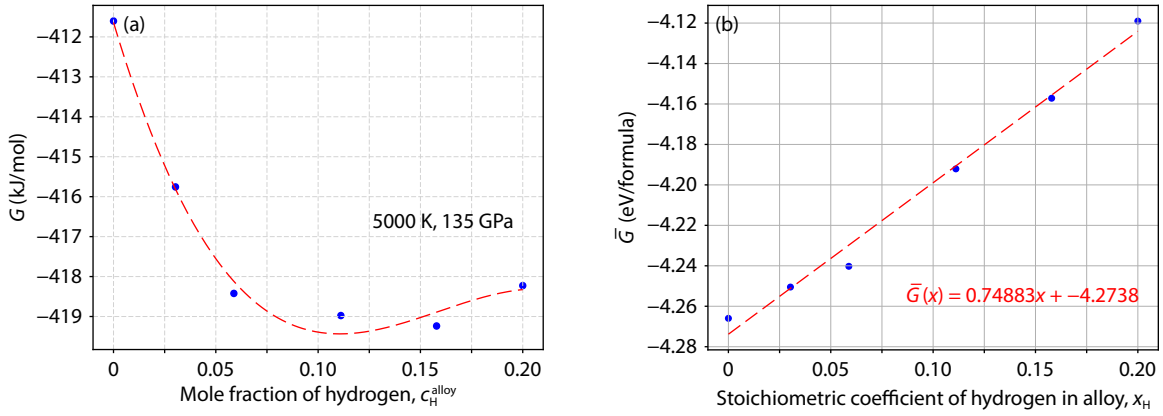

Figure S3. (a) Gibbs energy curves as functions of the hydrogen atomic fraction for the Fe-H reference systems. (b) The derived pure component Gibbs energy as functions of the stoichiometric coefficient of hydrogen in the formula $Fe_{1-x}H_x$ for alloy systems. The chemical potential curve is plotted in Figure 2a.

Table S1. Calculated molar volumes *V*, Helmholtz free energies *F*, and Gibbs energy *G* of alloy and silicate melts with hydrogen at 135 GPa, 5000 K.

System	*V* (cm³/mol)	*F* (kJ/mol)	*G* (kJ/mol)	μ_H (eV/atom)
$Fe_{74}O_{15}Si_8$	4.923	−1092.71945	−428.13112	—
$Fe_{74}O_{15}Si_8H_2$	4.845	−1084.18634	−430.0488	−5.0212
$Fe_{74}O_{15}Si_8H_4$	4.772	−1074.91435	−430.70805	−4.7312
$Fe_{74}O_{15}Si_8H_6$	4.707	−1066.25434	−430.8134	−4.5649
$Fe_{74}O_{15}Si_8H_9$	4.603	−1052.5592	−431.19492	−4.4026
$Fe_{74}O_{15}Si_8H_{12}$	4.508	−1039.4432	−430.90043	−4.2907
$Fe_{74}O_{15}Si_8H_{18}$	4.333	−1014.81985	−429.82869	−4.1391
Fe_{64}	5.166	−1109.0321	−411.6036	—
$Fe_{64}H_2$	5.059	−1098.78872	−415.75668	−5.0315
$Fe_{64}H_4$	4.949	−1086.50149	−418.42211	−4.7457
$Fe_{64}H_8$	4.728	−1057.1904	−418.97626	−4.4717
$Fe_{64}H_{12}$	4.539	−1032.02353	−419.23749	−4.3203
$Fe_{64}H_{16}$	4.371	−1008.26013	−418.22672	−4.2184
$Mg_{40}Si_{40}O_{120}H_1$	4.041	−858.97437	−313.43074	−4.5603
$Mg_{40}Si_{40}O_{120}H_2$	4.039	−858.6835	−313.47812	−4.2637
$Mg_{40}Si_{40}O_{120}H_4$	4.009	−855.75809	−314.5918	−3.9693
$Mg_{40}Si_{40}O_{120}H_6$	3.981	−852.3455	−314.88494	−3.7988
$Mg_{40}Si_{40}O_{120}H_8$	3.967	−851.30948	−315.74949	−3.6791
$Mg_{40}Si_{40}O_{120}H_{12}$	3.921	−845.64384	−316.3638	−3.5126
$Mg_{40}Si_{40}O_{120}H_{16}$	3.877	−840.19847	−316.86812	−3.3967
$Mg_{40}Si_{40}O_{120}H_{20}$	3.833	−834.25158	−316.75808	−3.3084
$Mg_{40}Si_{40}O_{120}H_{24}$	3.794	−829.49634	−317.3292	−3.2376

Data Availability

The simulated data are summarized in Table S1, and the raw datasets are available from the authors on request.

References

Badro, J., Côté, A. S., and Brodholt, J. P. (2014). A seismologically consistent compositional model of Earth's core. *Proc. Natl. Acad. Sci. USA*, *111*(21), 7542–7545. https://doi.org/10.1073/pnas.1316708111

Badro, J., Brodholt, J. P., Piet, H., Siebert, J., and Ryerson, F. J. (2015). Core formation and core composition from coupled geochemical and geophysical constraints. *Proc. Natl. Acad. Sci. USA*, *112*(40), 12310–12314. https://doi.org/10.1073/pnas.1505672112

Broadley, M. W., Bekaert, D. V., Piani, L., Füri, E., and Marty, B. (2022). Origin of

life-forming volatile elements in the inner Solar System. *Nature*, *611*(7935), 245–255. https://doi.org/10.1038/s41586-022-05276-x

Clesi, V., Bouhifd, M. A., Bolfan-Casanova, N., Manthilake, G., Schiavi, F., Raepsaet, C., Bureau, H., Khodja, H., and Andrault, D. (2018). Low hydrogen contents in the cores of terrestrial planets. *Sci. Adv.*, *4*(3), e1701876. https://doi.org/10.1126/sciadv.1701876

Fischer, R. A., Nakajima, Y., Campbell, A. J., Frost, D. J., Harries, D., Langenhorst, F., Miyajima, N., Pollok, K., and Rubie, D. C. (2015). High pressure metal–silicate partitioning of Ni, Co, V, Cr, Si, and O. *Geochim. Cosmochim. Acta*, *167*, 177–194. https://doi.org/10.1016/j.gca.2015.06.026

Garnero, E. J., McNamara, A. K., and Shim, S. H. (2016). Continent-sized anomalous zones with low seismic velocity at the base of Earth's mantle. *Nat. Geosci.*, *9*(7), 481–489. https://doi.org/10.1038/ngeo2733

Hacker, B. R. (2008). H_2O subduction beyond arcs. *Geochem. Geophys. Geosyst.*, *9*(3), Q03001. https://doi.org/10.1029/2007GC001707

Hirose, K., Labrosse, S., and Hernlund, J. (2013). Composition and state of the core. *Annu. Rev. Earth Planet. Sci.*, *41*(1), 657–691. https://doi.org/10.1146/annurev-earth-050212-124007

Hirose, K., Morard, G., Sinmyo, R., Umemoto, K., Hernlund, J., Helffrich, G., and Labrosse, S. (2017). Crystallization of silicon dioxide and compositional evolution of the Earth's core. *Nature*, *543*(7643), 99–102. https://doi.org/10.1038/nature21367

Hirose, K., Wood, B., and Vočadlo, L. (2021). Light elements in the Earth's core. *Nat. Rev. Earth Environ.*, *2*(9), 645–658. https://doi.org/10.1038/s43017-021-00203-6

Hirschmann, M. M. (2006). Water, melting, and the deep Earth H_2O cycle. *Annu. Rev. Earth Planet. Sci.*, *34*(1), 629–653. https://doi.org/10.1146/annurev.earth.34.031405.125211

Kresse, G., and Joubert, D. (1999). From ultrasoft pseudopotentials to the projector augmented-wave method. *Phys. Rev. B*, *59*(3), 1758–1775. https://doi.org/10.1103/PhysRevB.59.1758

Kuramoto, K., and Matsui, T. (1996). Partitioning of H and C between the mantle and core during the core formation in the Earth: Its implications for the atmospheric evolution and redox state of early mantle. *J. Geophys. Res.: Planets*, *101*(E6), 14909–14932. https://doi.org/10.1029/96JE00940

Li, Y. G., Vočadlo, L., Alfè, D., and Brodholt, J. (2019). Carbon partitioning between the Earth's inner and outer core. *J. Geophys. Res.: Solid Earth*, *124*(12), 12812–12824. https://doi.org/10.1029/2019JB018789

Li, Y. G., Vočadlo, L., Sun, T., and Brodholt, J. P. (2020). The Earth's core as a reservoir of water. *Nat. Geosci.*, *13*(6), 453–458. https://doi.org/10.1038/s41561-020-0578-1

Malavergne, V., Bureau, H., Raepsaet, C., Gaillard, F., Poncet, M., Surblé, S., Sifré, D., Shcheka, S., Fourdrin, C., … Khodja, H. (2019). Experimental constraints on the fate of H and C during planetary core–mantle differentiation. *Implications for the Earth. Icarus*, *321*, 473–485. https://doi.org/10.1016/j.icarus.2018.11.027

Mermin, N. D. (1965). Thermal properties of the inhomogeneous electron gas. *Phys. Rev.*, *137*(5A), A1441–A1443. https://doi.org/10.1103/PhysRev.137.A1441

Mueller, T., Hernandez, A., and Wang, C. H. (2020). Machine learning for interatomic potential models. *J. Chem. Phys.*, *152*(5), 050902. https://doi.org/10.1063/1.5126336

Okuchi, T. (1997). Hydrogen partitioning into molten iron at high pressure: Implications for Earth's core. *Science*, *278*(5344), 1781–1784. https://doi.org/10.1126/science.278.5344.1781

Pan, C. C., and He, X. B. (2023). Subducting passive continental margins with crustal (ultra)mafic intrusions: An underappreciated mechanism for recycling water back into the mantle. *Earth Planet. Phys.*, *7*(5), 576–581. https://doi.org/10.26464/epp2023074

Pearson, D. G., Brenker, F. E., Nestola, F., McNeill, J., Nasdala, L., Hutchison, M. T., Matveev, S., Mather, K., Silversmit, G., … Vincze, L. (2014). Hydrous mantle transition zone indicated by ringwoodite included within diamond. *Nature*, *507*(7491), 221–224. https://doi.org/10.1038/nature13080

Perdew, J. P., Burke, K., and Ernzerhof, M. (1996). Generalized gradient approximation made simple. *Phys. Rev. Lett.*, *77*(18), 3865–3868. https://doi.org/10.1103/PhysRevLett.77.3865

Pozzo, M., Davies, C., Gubbins, D., and Alfè, D. (2019). FeO content of Earth's liquid core. *Phys. Rev. X*, *9*(4), 041018. https://doi.org/10.1103/PhysRevX.9.041018

Samuel, H., Drilleau, M., Rivoldini, A., Xu, Z. B., Huang, Q. C., Garcia, R. F., Lekić, V., Irving, J. C. E., Badro, J., … Banerdt, W. B. (2023). Geophysical evidence for an enriched molten silicate layer above Mars's core. *Nature*, *622*(7984), 712–717. https://doi.org/10.1038/s41586-023-06601-8

Shibazaki, Y., Ohtani, E., Terasaki, H., Suzuki, A., and Funakoshi, K. I. (2009). Hydrogen partitioning between iron and ringwoodite: Implications for water transport into the Martian core. *Earth Planet. Sci. Lett.*, *287*(3-4), 463–470. https://doi.org/10.1016/j.epsl.2009.08.034

Stähler, S. C., Khan, A., Banerdt, W. B., Lognonné, P., Giardini, D., Ceylan, S., Drilleau, M., Duran, A. C., Garcia, R. F., … Smrekar, S. E. (2021). Seismic detection of the Martian core. *Science*, *373*(6553), 443–448. https://doi.org/10.1126/science.abi7730

Sun, T., Brodholt, J. P., Li, Y. G., and Vočadlo, L. (2018). Melting properties from *ab initio* free energy calculations: Iron at the Earth's inner-core boundary. *Phys. Rev. B*, *98*(22), 224301. https://doi.org/10.1103/PhysRevB.98.224301

Tagawa, S., Sakamoto, N., Hirose, K., Yokoo, S., Hernlund, J., Ohishi, Y., and Yurimoto, H. (2021). Experimental evidence for hydrogen incorporation into Earth's core. *Nat. Commun.*, *12*(1), 2588. https://doi.org/10.1038/s41467-021-22035-0

Thompson, A. P., Aktulga, H. M., Berger, R., Bolintineanu, D. S., Brown, W. M., Crozier, P. S., in't Veld, P. J., Kohlmeyer, A., Moore, S. G., … Plimpton, S. J. (2022). LAMMPS—A flexible simulation tool for particle-based materials modeling at the atomic, meso, and continuum scales. *Comput. Phys. Commun.*, *271*, 108171. https://doi.org/10.1016/j.cpc.2021.108171

Tkalčić, H., and Phạm, T. S. (2018). Shear properties of Earth's inner core constrained by a detection of *J* waves in global correlation wavefield. *Science*, *362*(6412), 329–332. https://doi.org/10.1126/science.aau7649

Tuckerman, M. E. (2023). *Statistical Mechanics: Theory and Molecular Simulation* (2nd ed). Oxford: Oxford University Press. https://doi.org/10.1093/oso/9780198825562.001.0001

Umemoto, K., and Hirose, K. (2015). Liquid iron-hydrogen alloys at outer core conditions by first-principles calculations. *Geophys. Res. Lett.*, *42*(18), 7513–7520. https://doi.org/10.1002/2015GL065899

Umemoto, K., and Hirose, K. (2020). Chemical compositions of the outer core examined by first principles calculations. *Earth Planet. Sci. Lett.*, *531*, 116009. https://doi.org/10.1016/j.epsl.2019.116009

Wang, H., Zhang, L. F., Han, J. Q., and E, W. N. (2018). DeePMD-kit: A deep learning package for many-body potential energy representation and molecular dynamics. *Comput. Phys. Commun.*, *228*, 178–184. https://doi.org/10.1016/j.cpc.2018.03.016

Zeng, J. Z., Zhang, D., Lu, D. H., Mo, P. H., Li, Z. Y., Chen, Y. X., Rynik, M., Huang, L., Li, Z. Y., … Wang, H. (2023). DeePMD-kit v2: A software package for deep potential models. *J. Chem. Phys.*, *159*(5), 054801. https://doi.org/10.1063/5.0155600

Zhang, L. F., Han, J. Q., Wang, H., Saidi, W. A., Car, R., and E, W. N. (2018). End-to-end symmetry preserving inter-atomic potential energy model for finite and extended systems. In *Proceedings of the 32nd International Conference on Neural Information Processing Systems* (pp. 4441–4451). Montréal, Canada: Curran Associates Inc.

Zhang, Y. G., and Yin, Q. Z. (2012). Carbon and other light element contents in the Earth's core based on first-principles molecular dynamics. *Proc. Natl. Acad. Sci. USA*, *109*(48), 19579–19583. https://doi.org/10.1073/pnas.1203826109

Zhang, Z. G., Csányi, G., and Alfè, D. (2020). Partitioning of sulfur between solid and liquid iron under Earth's core conditions: Constraints from atomistic simulations with machine learning potentials. *Geochim. Cosmochim. Acta*, *291*, 5–18. https://doi.org/10.1016/j.gca.2020.03.028

Zhang, Z. G., Csányi, G., Alfè, D., Zhang, Y. G., Li, J., and Liu, J. (2022a). Free energies of Fe-O-Si ternary liquids at high temperatures and pressures: Implications for the evolution of the Earth's core composition. *Geophys. Res. Lett.*, *49*(4), e2021GL096749. https://doi.org/10.1029/2021GL096749

Zhang, Z. G., Liu, J., Zhang, Y. G., and Li, J. (2022b). Coexistence simulations of silicate melts and liquid iron and the exchanges of oxygen between the Earth's mantle and core. *Chin. J. Geophys. (in Chinese)*, *65*(11), 4249–4258. https://doi.org/10.6038/cjg2022Q0749

Zhou, S. Y., Liu, D. H., Zhang, C. Y., Wang, X. B., and Song, L. (2025). *Ab initio* molecular dynamics investigation of the proton conductivity and dynamics behavior of hydrous ringwoodite under high temperatures and pressure. *Earth Planet. Phys.*, *9*(4), 842–852. https://doi.org/10.26464/epp2025049

Zwillinger, D. (2002). *CRC Standard Mathematical Tables and Formulae* (31st ed). New York: Chapman and Hall/CRC. https://doi.org/10.1201/9781420035346